Supplemental Information: J-freezing and Hund's rules in spin-orbit-coupled multiorbital Hubbard models

Aaram J. Kim,[1] Harald O. Jeschke,[1] Philipp Werner,[2] and Roser Valentí[1]

[1]*Institut für Theoretische Physik, Goethe-Universität Frankfurt,*
Max-von-Laue-Straße 1, 60438 Frankfurt am Main, Germany
[2]*Department of Physics, University of Fribourg, Chemin du Musée 3, 1700 Fribourg, Switzerland*

J_z correlation function and local susceptibility

In this section, we illustrate the correlation functions which are the basic tool for investigating the phase diagram of the three-band Hubbard model with spin-orbit coupling. Figure S1 presents the local correlation function of the total moment J_z and the corresponding susceptibility for two different fillings, $n = 2$ and 4. Figure 1 in the main text and Fig. S2 are constructed based on these correlation functions. The instantaneous value of the correlation function, $\langle J_z^2 \rangle$, is determined by the size of the local moment and the right most value, $\langle J_z(\beta/2)J_z \rangle$, estimates the long-term memory for a given temperature scale. The local susceptibility χ_{loc} (Eq. (4) in the main text) and its dynamic contribution $\Delta\chi_{\text{loc}}$ (Eq. (5) in the main text) are graphically illustrated in Fig. S1 (a).

In the $n = 2$ case, the correlation function and the susceptibility show a monotonic behavior. As strong Coulomb interactions localize the electrons, both the size of the local moment and its long-term memory increase simultaneously. The increase in both quantities contributes to the susceptibility. However, the dynamic contribution shows a peak at an intermediate interaction value (Fig. S1 (c)). Compared to the noninteracting limit, the enhanced correlations and slow decay of the moment result in a larger value of $\Delta\chi_{\text{loc}}$, but this quantity again vanishes in the fully localized
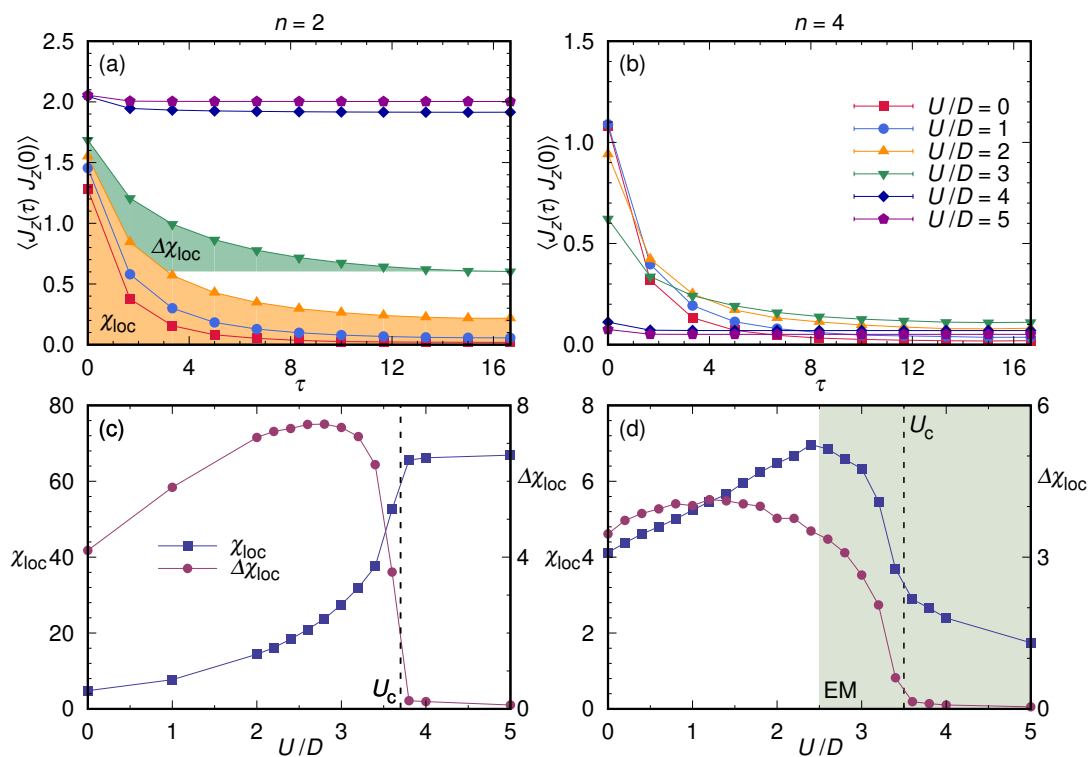

Figure S1: (a), (b) Dynamical correlation function of the total moment J_z for various U/D values. (c,d) The susceptibility and its dynamical contribution as a function of U/D. (c), (d) The vertical dashed lines mark the critical interaction strength U_c of the metal-insulator-transition. The green shading in (d) represents the excitonic AFM region. The left and right columns show the $n = 2$ and $n = 4$ results, respectively. $\lambda/D = 0.25$, $J_H/U = 0.15$, and $T/D = 0.03$ for all panels. The color scheme is fixed within the same row. χ_{loc} and $\Delta\chi_{\text{loc}}$ are graphically represented in panel (a).
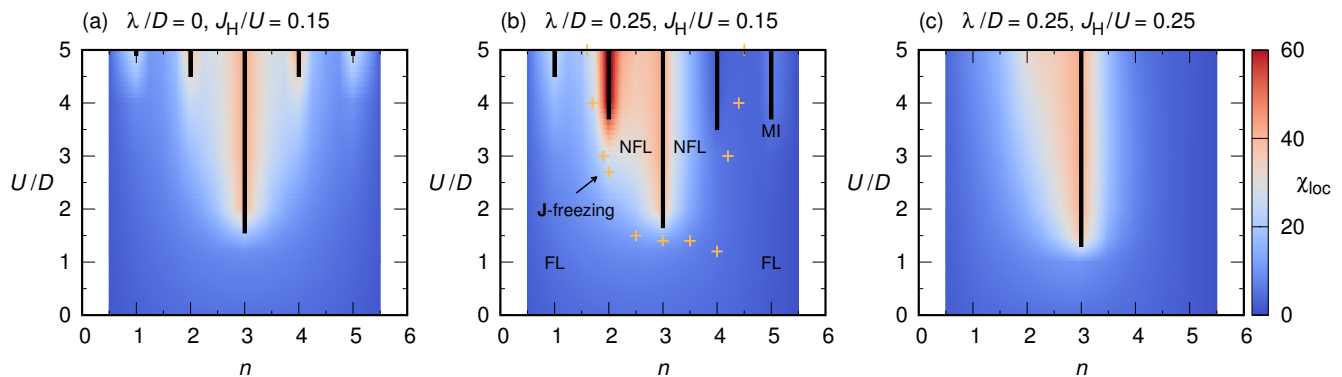
Figure S2: Local susceptibility in the $(U/D, n)$ phase diagram for (a) $\lambda/D = 0.0$, $J_{\mathrm{H}}/U = 0.15$, (b) $\lambda/D = 0.25$, $J_{\mathrm{H}}/U = 0.15$, (c) $\lambda/D = 0.25$, $J_{\mathrm{H}}/U = 0.25$, and $T/D = 0.03$. Cross symbols mark the maximum values of $\Delta\chi_{\mathrm{loc}}$ (compare Figs. S1 (c) and (d)) which may be used to define the **J**-freezing crossover points.

limit. Hence, a peak in $\Delta\chi_{\mathrm{loc}}$ can be naturally expected as a function of U.

On the other hand, the behavior of the local susceptibility is nonmonotonic in the $n = 4$ case. The long-term memory of the correlation function and the susceptibility show a peak structure in the intermediate interaction regime. The strong suppression of the susceptibility in the localized phase, which may be attributed to the nonmagnetic character of the Van-Vleck-type ground state (vanishing **J**-moments) leads to this peak structure. The form of the ground state is shown in Table SII. In other words, the small peak in χ_{loc} is the result of a competition between **J**-freezing and quenching of the local moment. If symmetry breaking is allowed, the antiferromagnetic and excitonic order extend into the region with enhanced local spin susceptibility. In this sense, we may regard the fluctuating local moments in this crossover regime as the hosting background for the symmetry-broken states.

The very different behaviors of the susceptibility in the $n = 2$ and 4 cases are illustrated in Fig. S2. Compared to the non-spin-orbit-coupled system, Fig. S2 (a), the enhancement at $n = 2$ and the suppression at $n = 4$ of the local susceptibility in and near the localized phase are clearly evident in Fig. S2 (b). These strong effects persist into the intermediate coupling regime and for doped systems, as shown in Figs. S2 (b) and (c). The susceptibility of the itinerant phase with $n = 2$ is much larger than for $n = 4$.

It is interesting to analyze the different contributions to the total moment correlation function in the J-freezing region. The correlation function of the J_z-moment can be expressed as

$$\langle J_z(\tau)J_z(0)\rangle = \langle L_z(\tau)L_z(0)\rangle + \langle S_z(\tau)S_z(0)\rangle + \langle L_z(\tau)S_z(0)\rangle + \langle S_z(\tau)L_z(0)\rangle \ . \tag{1}$$

Figure S3 shows the J_z-correlation function and its individual terms for several different fillings. When considering fillings which are symmetric relative to $n = 3$, for example $n = 2$ and 4 (or $n = 2.5$ and 3.5), one notices that the difference in the J_z-correlations function mainly comes from the opposite sign in the L_z-S_z contributions. On the other hand, the L_z- and S_z-correlation functions are very similar for both fillings.

As the system gets closer to half-filling, the contribution of the S_z-correlation function increases while that of the L_z and L_z-S_z correlation function is suppressed. The dominant contribution of the S_z correlation function at $n = 2.5$ and 3.5 can be attributed to the effect of the atomic ground state at $n = 3$ with a spin-maximized and orbital-singlet state. This analysis suggests that the flavor-averaged value of the scattering rate at the Fermi-level is mostly determined by the spin correlation function and that the similar values of the dominant S_z-correlation function for symmetric fillings result in similar values of the average scattering rate. This is indeed the case as can be seen in Fig. 3 of the main text.

Local Hamiltonian

The local Hamiltonian not only describes the physical properties of the fully localized limit but also affects the properties of the correlated itinerant phases. In our model, the local Hamiltonian is composed of two terms: the SOC and the Kanamori-type Coulomb interaction,

$$\mathcal{H}_{\mathrm{loc}} = \mathcal{H}_\lambda + \mathcal{H}_{\mathrm{int}} \ . \tag{2}$$

Using the total electron number N and the total moment J_z as quantum numbers, we diagonalized $\mathcal{H}_{\mathrm{loc}}$. Tables SI and SII summarize the properties of the ground states for each N. In Table SI, the numbers in parenthesis are the
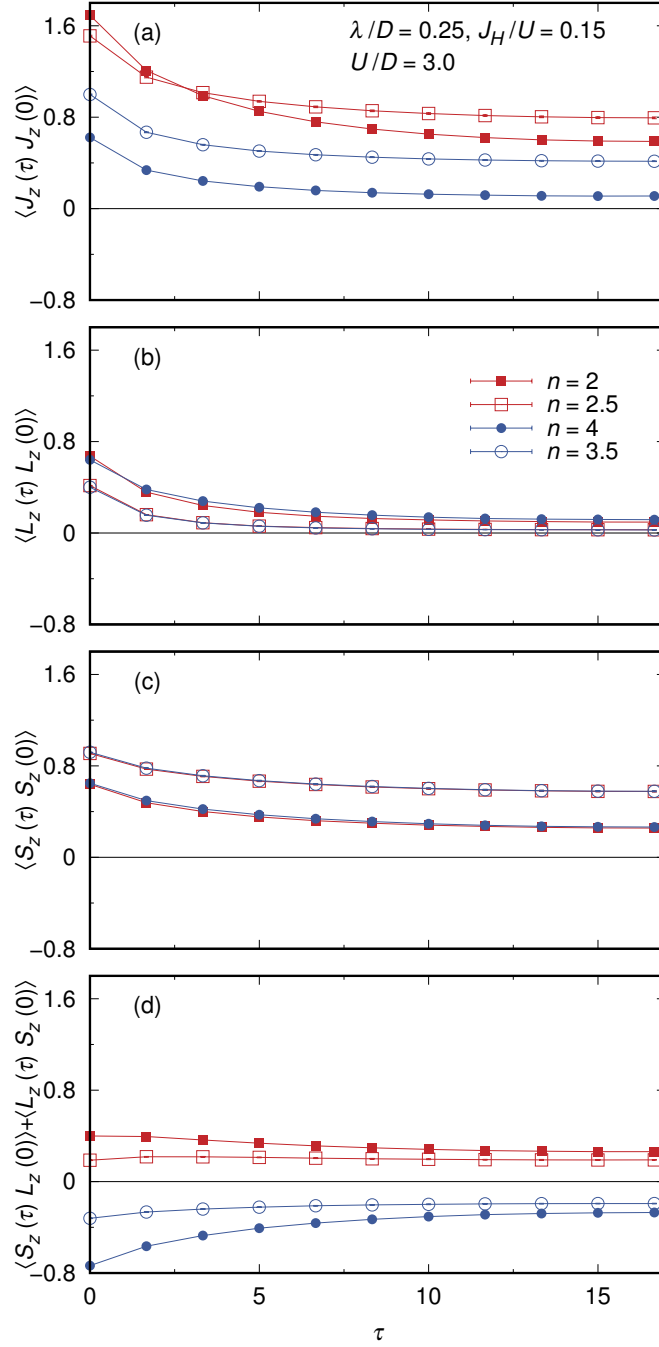
Figure S3: Various correlation functions for $\lambda/D = 0.25$, $J_{\mathrm{H}}/U = 0.15$, $U/D = 3$, and $T/D = 0.03$. From top to bottom, the corresponding functions are the auto-correlation functions of the J_z, L_z, and S_z moment, and the cross-correlation function between the S_z and L_z moment.

ground state degeneracies of the non-spin-orbit-coupled Hamiltonian and μ is the chemical potential. As we turn on the SOC, the degeneracy is reduced except for $N = 3$, which means that the average kinetic energy is reduced, as discussed in the main text. Based on the ground state energy, we calculate the charge gap, defined by

$$\Delta_{\mathrm{ch}}(N) = (E_{\mathrm{g}}(N+1) - E_{\mathrm{g}}(N)) - (E_{\mathrm{g}}(N) - E_{\mathrm{g}}(N-1)) \; , \tag{3}$$

where $E_{\mathrm{g}}(N)$ is the ground state energy of the local Hamiltonian for filling N. The results are summarized in Table SIII, and Fig. S4 represents $\delta\Delta_{\mathrm{ch}}(N, J_{\mathrm{H}}, \lambda) \equiv \Delta_{\mathrm{ch}} - U$. The summary of the Hund's rules which apply to the local Hamiltonian is also presented in Table SIV.

N	Degeneracy	Ground State Energy (E_g)
0	1 (1)	0
1	4 (6)	$-\frac{\lambda}{2} - \mu$
2	5 (9)	$\frac{1}{4}\left(4U - 8J_\mathrm{H} - \lambda - \sqrt{16J_\mathrm{H}^2 + 8J_\mathrm{H}\lambda + 9\lambda^2}\right) - 2\mu$
3	4 (4)	$3U + f(J_\mathrm{H}, \lambda) - 3\mu$
4	1 (9)	$\frac{1}{2}\left(12U - 21J_\mathrm{H} - \lambda - \sqrt{25J_\mathrm{H}^2 + 10J_\mathrm{H}\lambda + 9\lambda^2}\right) - 4\mu$
5	2 (6)	$10U - 20J_\mathrm{H} - \lambda - 5\mu$
6	1 (1)	$15U - 30J_\mathrm{H} - 6\mu$

Table SI: Ground state energy and degeneracy of the local Hamiltonian for different total particle numbers. The numbers in the parentheses show the ground state degeneracies when $\lambda = 0$.

Table SII: Ground state for a given sector of the local Hamitonian. In our notation, the upper (lower) level represents the $j = 1/2$ (3/2) states and the lower left (right) level corresponds to $m_j = \pm 1/2$ ($m_j = \pm 3/2$). Full (empty) circles mark the positive (negative) m_j electron. All coefficients can be chosen to be real and duplicated symbols in different sectors have nothing to do with each other.

Figures S4 (b) through (f) illustrate the effect of the SOC on the charge gap, which turns out to be different for different N. In the regime of interest, finite J_H and relatively small λ, $\delta\Delta_\mathrm{ch}$ is an increasing function of λ for $N = 1$, 2 and 4, but a decreasing function for $N = 3$ and 5. Based on the information of the degeneracy and charge gap, we discuss the qualitative behavior of the critical interaction strength U_c in the main text.

N	Charge Gap (Δ_{ch})
1	$U - 2J_{\mathrm{H}} + \frac{3\lambda}{4} - \frac{1}{4}\sqrt{16J_{\mathrm{H}}^2 + 8J_{\mathrm{H}}\lambda + 9\lambda^2}$
2	$f(J_{\mathrm{H}}, \lambda) + U + 4J_{\mathrm{H}} + \frac{1}{2}\sqrt{16J_{\mathrm{H}}^2 + 8J_{\mathrm{H}}\lambda + 9\lambda^2}$
3	$U - \frac{25J_{\mathrm{H}}}{2} - \frac{3\lambda}{4} - \frac{1}{4}\sqrt{16J_{\mathrm{H}}^2 + 8J_{\mathrm{H}}\lambda + 9\lambda^2} - \frac{1}{2}\sqrt{25J_{\mathrm{H}}^2 + 10J_{\mathrm{H}}\lambda + 9\lambda^2} - 2f(J_{\mathrm{H}}, \lambda)$
4	$f(J_{\mathrm{H}}, \lambda) + U + J_{\mathrm{H}} + \sqrt{25J_{\mathrm{H}}^2 + 10J_{\mathrm{H}}\lambda + 9\lambda^2}$
5	$U - \frac{J_{\mathrm{H}}}{2} - \frac{\lambda}{2} - \frac{1}{2}\sqrt{25J_{\mathrm{H}}^2 + 10J_{\mathrm{H}}\lambda + 9\lambda^2}$

Table SIII: Charge gap for different total particle numbers. Note that Δ_{ch} can be expressed as $U + \delta\Delta_{\mathrm{ch}}(N, J_{\mathrm{H}}, \lambda)$. We do not specify $f(J_{\mathrm{H}}, \lambda)$ because it is difficult to express it in a simple form. Numerical values are used to obtain Fig. S4.

n	S	L	J
1	$1/2$	1	$3/2$
2	1	1	2
3	$3/2$	0	$3/2$
4	1	1	0
5	$1/2$	1	$1/2$

Table SIV: Summary of Hund's rules including the third law.

Energy Scales in Various Materials

In Tab. SV, we summarize the previous estimates of the energy scales for various materials. Our main parameter set is chosen to be the estimate from Sr_2IrO_4 [1]. The absolute value of the SOC is mainly determined by the relevant atom; 0.1~0.2 eV for Ru, Rh and 0.3~0.4 eV for Os, Ir. In these materials, the Hund's coupling strength; J_H/U varies within 0.1~0.22 which is the range considered in our calculations.
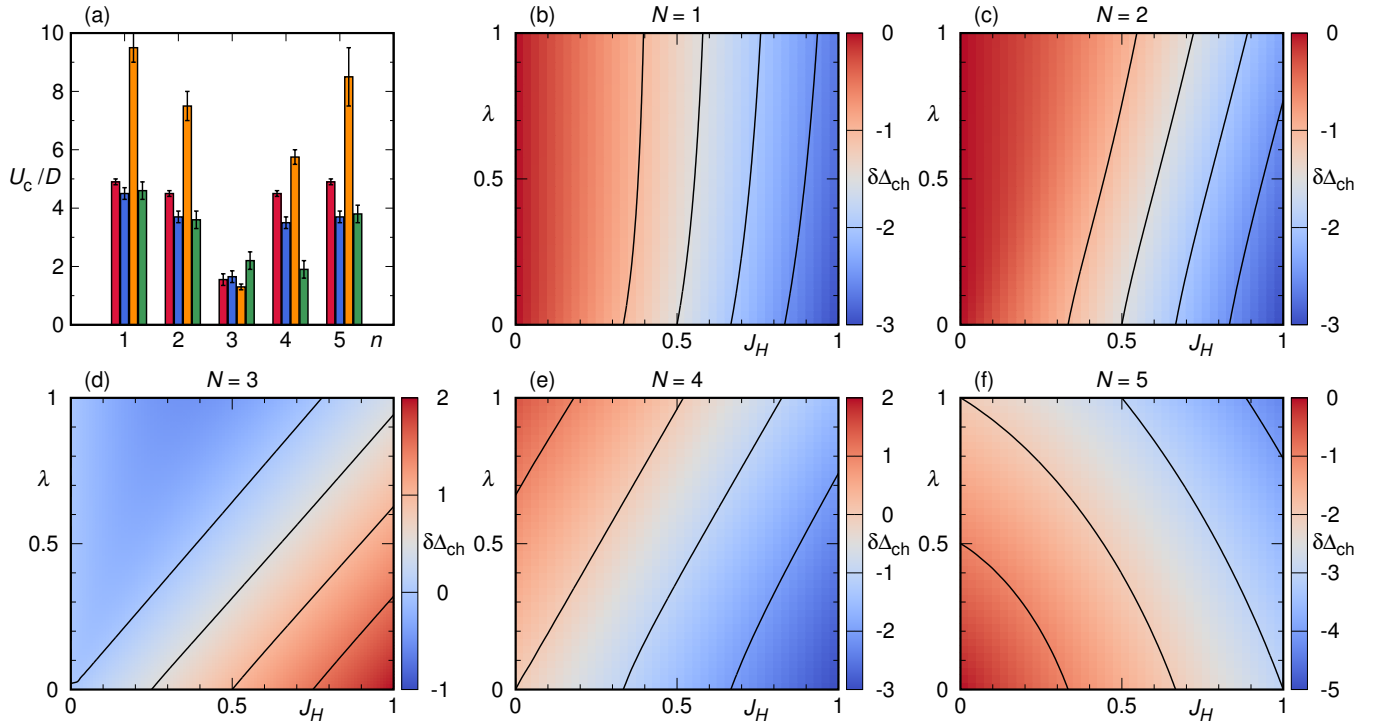
Figure S4: (a) Critical interaction strength U_c as a function of electron filling. From left to right within a group of four bars, the bars represents the U_c for $(\lambda, J_H/U) = (0, 0.15), (0.25, 0.15), (0.25, 0.25)$, and $(0.5, 0.15)$, respectively. (b)-(f) Density plot of $\delta\Delta_{\mathrm{ch}}$ as a function of J_H and λ for different total particle number N. $\delta\Delta_{\mathrm{ch}}(N, J_H, \lambda)$ is defined as $\Delta_{\mathrm{ch}} - U$.

Material	Conf.	D	λ/D	J_H/U	U/D	Ref.
Sr_2IrO_4	d^5	1.44eV	0.257 (0.37eV)	0.15	-	[1]
Sr_2RhO_4	d^5	1.44eV	0.125 (0.18eV)	0.15	-	[1]
$Y_2Ir_2O_7$	d^5	0.5eV	0.8 (0.4eV)	0.1	5.0 (2.5eV)	[2]
Na_2IrO_3 Li_2IrO_3 α-$RuCl_3$	d^5	0.2eV	2.0 (0.4eV) 0.75 (0.15eV)	0.2	15 (3eV)	[3]
Sr_2RuO_4	d^4	0.75eV	0.13 (0.100eV)	-	-	[4]
Sr_2YRuO_6	d^4	0.55eV	0.18 (0.100eV)	0.20	4.73 (2.6eV)	[5–7]
Sr_2YIrO_6 Ba_2YIrO_6	d^4	0.5eV	0.6 (0.33eV)	0.22	3.6 (1.8eV)	[8]
Sr_2CrOsO_6	d^3	0.75eV	0.4 (0.3eV)	0.17	2.67 (2eV)	[9]
Ba_2NaOsO_6	d^1	0.3eV	1.0 (0.3eV)	-	-	[10, 11]

Table SV: Summary of the energy scales in various spin-orbit-coupled materials. D, λ, J_H, and U are the half-bandwidth, strength of spin-orbit coupling, Hund's coupling, and Coulomb interaction, respectively.

Long-Range Order near $n = 4$

For large Hund's coupling and small SOC, we observe itinerant FM. In Fig. S5, the increase of the SOC results in successive phase transitions from FM to AFM, and from AFM to PM. For a given total moment $\langle \mathbf{J} \rangle$, the internal structure is different depending on the magnetic phase. In the FM phase, $\langle \mathbf{S} \rangle$ and $\langle \mathbf{L} \rangle$ are aligned in the same direction, and $\langle \mathbf{S} \rangle$ makes the dominant contribution to $\langle \mathbf{J} \rangle$. On the other hand, in the AFM phase, $\langle \mathbf{S} \rangle$ and $\langle \mathbf{L} \rangle$ are anti-aligned, but $\langle \mathbf{L} \rangle$ dominates $\langle \mathbf{S} \rangle$.

Our results show that the Hund's coupling enhances the FM while the SOC suppresses it. This behavior is consistent with the previous results [5, 12], especially two-site Exact diagonalization (ED) results in Fig. S6. Assuming a square lattice, the value of the critical strength of the SOC, $\lambda_c/D = 0.1275$ for $J_H/D = 0.25$ in the ED results is compatible with our DMFT results.

[1] H. Watanabe, T. Shirakawa, and S. Yunoki, Phys. Rev. Lett. **105**, 216410 (2010).
[2] H. Shinaoka, S. Hoshino, M. Troyer, and P. Werner, Phys. Rev. Lett. **115**, 156401 (2015).
[3] S. M. Winter, Y. Li, H. O. Jeschke, and R. Valentí, Phys. Rev. B **93**, 214431 (2016).
[4] M. W. Haverkort, I. S. Elfimov, L. H. Tjeng, G. A. Sawatzky, and A. Damascelli, Phys. Rev. Lett. **101**, 026406 (2008).
[5] O. N. Meetei, W. S. Cole, M. Randeria, and N. Trivedi, Phys. Rev. B **91**, 054412 (2015).
[6] L. Vaugier, H. Jiang, and S. Biermann, Phys. Rev. B **86**, 165105 (2012).
[7] I. I. Mazin and D. J. Singh, Phys. Rev. B **56**, 2556 (1997).
[8] K. Pajskr, P. Novák, V. Pokorný, J. Kolorenč, R. Arita, and J. Kuneš, Phys. Rev. B **93**, 035129 (2016).
[9] O. N. Meetei, O. Erten, M. Randeria, N. Trivedi, and P. Woodward, Phys. Rev. Lett. **110**, 087203 (2013).
[10] S. Gangopadhyay and W. E. Pickett, Phys. Rev. B **93**, 155126 (2016).
[11] K.-W. Lee and W. E. Pickett, EPL (Europhysics Letters) **80**, 37008 (2007).
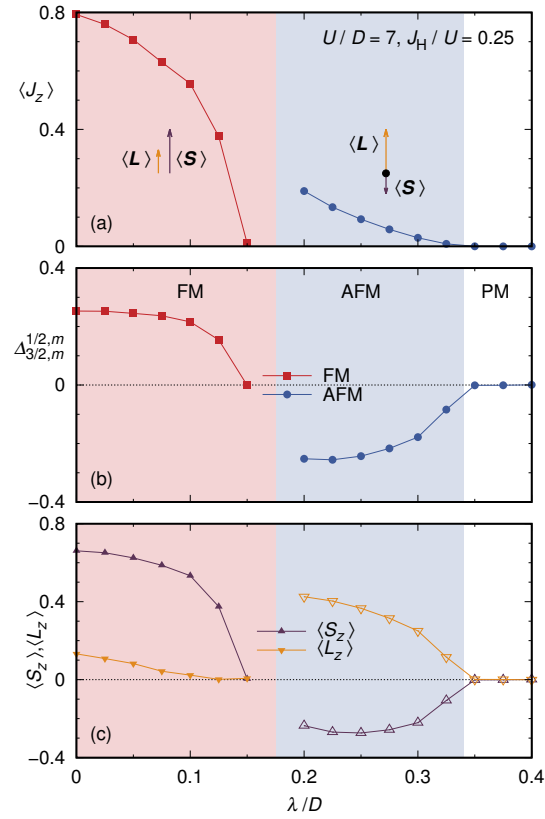[12] J. Chaloupka and G. Khaliullin, Phys. Rev. Lett. **116**, 017203 (2016).

Figure S5: (a) Total magnetic moment, (b) excitonic order parameter and (c) spin/orbital moment as a function of λ/D for $T/D = 0.33$, $n = 4$, $J_{\mathrm{H}}/U = 0.25$, and $U/D = 7$. The red (blue) shading represents the FM (AFM) region. The arrows in (a) show the alignment (anti-alignment) of spin and orbital moment in the FM (AFM) region.
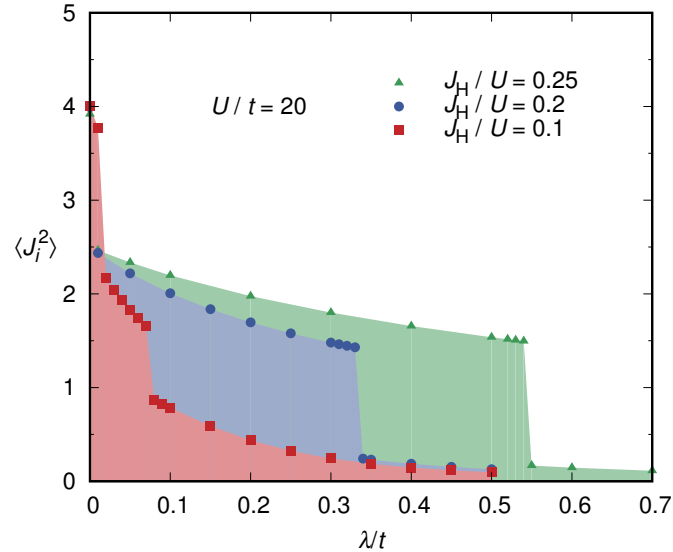

Figure S6: The size of the total moment for a given site in the two-site Hubbard model as a function of λ/t for $U/t = 20$. Here t is the hopping parameter between two sites. From top to bottom, the corresponding Hund's coupling strengths are 0.25, 0.2, and 0.1, respectively.